

Firm Detection of a Cyclotron Resonance Feature with Suzaku in the X-ray Spectrum of GRO J1008–57 during a Giant Outburst in 2012

Takayuki YAMAMOTO,¹ Tatehiro MIHARA,¹ Mutsumi SUGIZAKI,¹ Motoki NAKAJIMA,² Kazuo MAKISHIMA,^{1,3}
and Makoto SASANO³

¹MAXI team, RIKEN, 2-1 Hirosawa, Wako, Saitama 351-0198
tyamamot@crab.riken.jp

²School of Dentistry at Matsudo, Nihon University, 2-870-1 Sakaecho-nishi, Matsudo, Chiba 101-8308

³Department of Physics, The University of Tokyo, 7-3-1 Hongo, Bunkyo, Tokyo 113-0033

(Received 2013 November 29; accepted 2014 January 18)

Abstract

We report on the firm detection of a cyclotron resonance scattering feature (CRSF) in the X-ray spectrum of the Be X-ray binary pulsar, GRO J1008–57, achieved by the Suzaku Hard X-ray Detector during a giant outburst which was detected by the MAXI Gas Slit Camera in 2012 November. The Suzaku observation was carried out on 2012 November 20, outburst maximum when the X-ray flux reached ~ 0.45 Crab in 4–10 keV, which corresponds to a luminosity of 1.1×10^{38} erg s^{−1} in 0.5–100 keV at 5.8 kpc. The obtained broadband X-ray spectrum from 0.5 keV to 118 keV revealed a significant absorption feature, considered as the fundamental CRSF, at ~ 76 keV. This unambiguously reconfirm the previously suggested ~ 80 keV spectral feature in GRO J1008–57. The implied surface magnetic field, 6.6×10^{12} G, is the highest among binary X-ray pulsars from which CRSFs have ever been detected.

Key words: stars: magnetic fields — pulsars: individual (GRO J1008–57) — stars: neutron — X-rays: binaries

1. Introduction

Pulsars, which exhibit pulsating electromagnetic radiations in various wavelength, are strongly magnetized neutron stars. The rotation of the neutron star, combined with anisotropic radiation, causes the periodic pulsation. Although they are considered to be formed by supernova explosions of massive stars, the origin and time evolution of their magnetic fields are still open questions.

X-ray binary pulsars (XBPs) are a group of X-ray binaries involving pulsating neutron stars. According to the type of the binary companion, they are classified into several subgroups including Super Giant XBPs and Be XBPs as major members (e.g. Reig 2011). Be XBPs produce recurrent outbursts synchronized with their binary orbital periods. The outbursts are considered to occur when the neutron star crosses a gaseous stellar disk of the Be star near the periastron passage. The outburst does not always appear every orbital cycle, and sometime arises in an irregular orbital phase, probably depending on the physical extent of the stellar disk.

Surface magnetic fields of neutron stars in XBPs can be estimated from the cyclotron resonance scattering feature (CRSF), which has been observed as absorption features in their X-ray spectra. The CRSF is considered to appear at an energy of $E_a = 11.6(1 + z_g)^{-1} B_{12}$, where B_{12} is the magnetic field strength in 10^{12} G, and z_g represents the gravitational redshift. Ginga/LAC observations in the 2–60 keV band detected the CRSFs from 12 XBPs and showed that their surface magnetic fields are distributed in a very narrow range of $(1.0 - 3.2) \times 10^{12}$ G (Mihara et al. 1998, Makishima et al. 1999). Subsequently, ASCA, RXTE, BeppoSAX, INTEGRAL and Suzaku observations surveyed a wider energy band from

~ 0.5 keV upto a few hundreds keV, and detected CRSFs from additional six XBPs (e.g. Coburn et al. 2002; Filippova et al. 2007; Doroshenko et al. 2010; Yamamoto et al. 2011; Tsygankov et al. 2012; DeCesar et al. 2013). However, the revised range of their surface magnetic fields, $(1.0 - 4.7) \times 10^{12}$ G, is still narrow. It is yet to be clarified whether this is intrinsic to XBPs, or a selection effect due to limited observations.

GRO J1008–57 is a Be XBP with a pulsation period of 93.5 s, discovered by the CGRO/BATSE in 1993 (Stollberg et al. 1993). Its optical counterpart was identified with a B0e type star (Coe et al. 1994) and the distance was estimated to be 5.8 kpc (Riquelme et al. 2012). Its X-ray outbursts have been monitored for about 20 years by surveys with the CGRO/BATSE, RXTE/ASM, Swift/BAT, and MAXI/GSC. Since 2003 January, the source has been in an active state exhibiting outbursts periodically (Kühnel et al. 2013). From the recurrent outburst intervals and the pulsar period modulation, the binary orbital period was estimated as 247.8 ± 0.4 d (Coe et al. 2007), which was recently refined to 249.48 ± 0.04 d by the pulse arrival-time analysis (Kühnel et al. 2013).

Based on the CGRO/OSSE pointing observations performed in the 1993 outburst and the BATSE earth-occultation data on that occasion, Shrader et al. (1999) suggested a possible CRSF at around 88 keV in the X-ray spectra of GRO J1008–57. In contrast, spectra of the 2004 outburst obtained by the INTEGRAL/IBIS and JEM-X showed no feature in the 3–60 keV band (Coe et al. 2007). Therefore, the possible absorption feature at 88 keV is considered to be the fundamental if it is real. Observations of the 2007 November outburst by RXTE, Swift, and Suzaku were unable to confirm the suggestion, hampered by rather poor signal statistics (Naik et al. 2011; Kühnel et al. 2013).

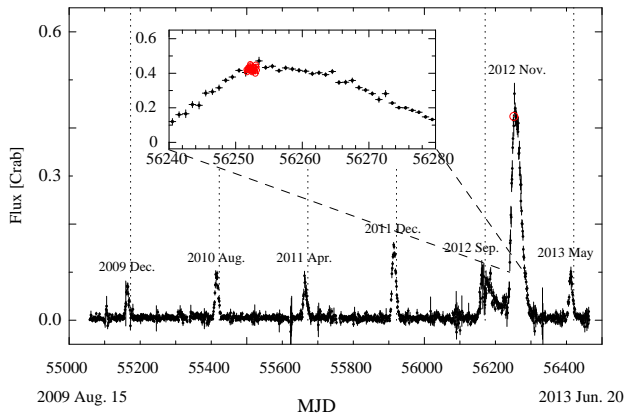


Fig. 1. MAXI/GSC light curve of GRO J1008–57 in the 4–10 keV band from 2009 August 15 to 2012 June 20. Vertical dash lines indicate the predicted epochs of periastron passage of the pulsar (Kühnel et al. 2013). The inset zooms up the profile of the outburst in 2012 November, on which Suzaku data taken on 2012 November 20–22 are superposed with circles.

In the present paper, we report the Suzaku observation performed at the peak of a giant outburst detected by MAXI in 2012 November, and the results of the spectral analysis for the CRSF. Unless otherwise specified, all errors hereafter refer to 90% confidence limits.

2. Outburst Activity Monitored by MAXI

MAXI (Matsuoka et al. 2009) Gas Slit Camera (GSC; Mihara et al. 2011) has been monitoring the X-ray flux of GRO J1008–57 since the operation started on 2009 August 15 (MJD=55058) (Sugizaki et al. 2011). Figure 1 shows the obtained light curve until 2013 June (MJD~56450). By 2012 September (MJD~56200), five outbursts were detected periodically at the same orbital phase close to the pulsar periastron passage. Their peak intensities in 4–10 keV are almost same at 0.1 Crab, which corresponds to a 0.5–100 keV luminosity of $L_X \simeq 2 \times 10^{37} \text{ erg s}^{-1}$ at 5.8 kpc assuming the same spectral shape as in Suzaku observation (section 3.4). Thus, these outbursts are categorized into the normal-type ones (Reig 2011). On 2012 November 5, the source exhibited unexpected brightening at an irregular orbital phase which is ~ 0.3 cycle after the periastron (Nakajima et al. 2012). The 4–10 keV intensity reached ~ 0.45 Crab at the maximum. Judging from the outburst phase and the peak luminosity, it is categorized into the giant-type outburst (Reig 2011).

3. Suzaku Observation of 2012 Giant Outburst and Data Analysis

3.1. Observation and Data Reduction

Triggered by the MAXI detection of the giant outburst from GRO J1008–57, we requested a Suzaku ToO (Target of Opportunity) observation. It was performed on 2012 November 20, nearly coincident with the outburst maximum. Suzaku covers an energy band from 0.5 to 500 keV with the X-ray Imaging Spectrometer (XIS: Koyama et al. 2007) and the Hard X-ray Detector (HXD: Takahashi et al. 2007, Kokubun

et al. 2007). The target was placed at the XIS nominal position on the focal-plane. The XIS was operated in the normal mode with 1/4-window and 0.3 s burst options, which affords a time resolution of 2 s. The HXD was operated in the nominal mode. Table 1 summarizes the Suzaku observations including exposure and count rate in each instrument.

The data reduction and analysis were performed with the standard procedure using the Suzaku analysis software in HEASOFT version 6.12 and the CALDB files version 20110913, provided by the NASA/GSFC Suzaku GOF. All obtained data were first reprocessed by a Suzaku software tool, *aepipeline* to utilize the latest calibration. The net exposures after the standard event-screening process were 18.1 ks with the XIS and 50.4 ks with the HXD. Due to the 0.3 s burst option, the XIS exposure is about one third of that of the HXD.

We started the XIS data analysis with the standard cleaned event files. On-source event data were collected from a circular region of $240''$ radius around the source position on the XIS CCD images, and background data from an annulus with the inner and outer radii of $300''$ and $420''$, respectively. The pileup effect on each image pixel was estimated by the Suzaku PileupTools¹. We excluded pixels on the image core in which the estimated pileup fraction is larger than 1% (Yamada et al. 2012).

In the HXD data analysis, we created the background spectra with the standard procedure, using the archived background files provided by the Suzaku GOF. The obtained HXD-PIN background includes contribution from the Cosmic X-ray Background (CXB), while it is negligible in the HXD-GSO data (Fukazawa et al. 2009). After subtracting the backgrounds, the source count rates became $14.61 \pm 0.01 \text{ counts s}^{-1}$ in the PIN 20–60 keV band, and $0.90 \pm 0.02 \text{ counts s}^{-1}$ in the GSO 60–115 keV band.

3.2. Timing Analysis

With the Suzaku analysis tool, *aebarycen*, we converted the photon arrival times of all events into those at the solar-system barycenter and then searched the data for the coherent pulsation by epoch-folding analysis. The $\sim 93.5 \text{ s}$ pulsation was detected significantly, both with the XIS and the HXD, and the best period was obtained as $93.6257 \pm 0.0001 \text{ s}$ with the HXD-PIN data. Figure 2 shows the folded pulse profiles in the XIS, HXD-PIN and HXD-GSO energy bands, where the phase $\phi = 0$ is set at the minimum in the HXD-PIN profile. We divided the HXD-GSO band into three, 50–70 keV, 70–80 keV and 80–100 keV, around the CRSF energy (section 3.3). The 50–70 keV profile is the same as that of HXD-PIN, while that in 70–80 keV is somewhat different. The pulsation is still significant in the highest energy band of 80–100 keV.

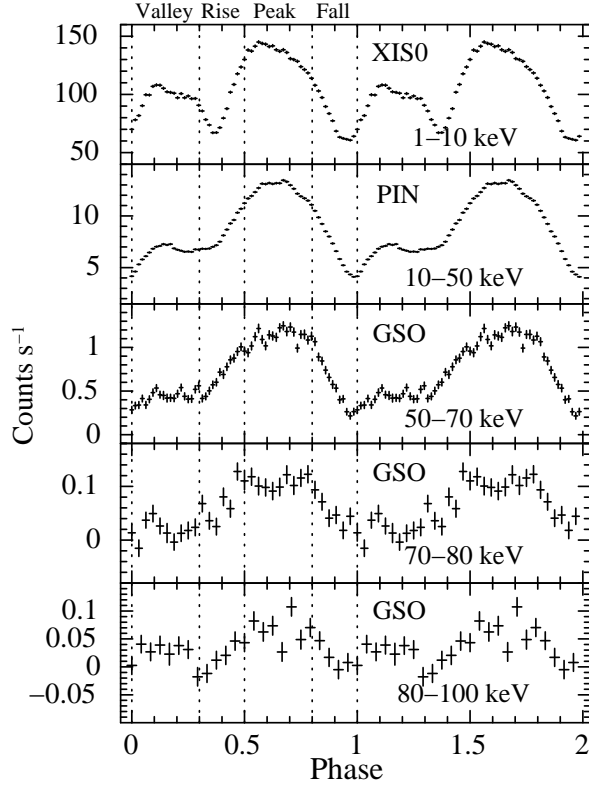
The pulse profile in the XIS has two peaks at $\phi \sim 0.1$ and $\phi \sim 0.6$. The former tends to decrease towards higher energies. These double-peak profiles and their energy dependence are largely consistent with the results obtained in previous outbursts (Shrader et al. 1999; Coe et al. 2007; Naik et al. 2011; Kühnel et al. 2013). However, details are rather different. Comparing the XIS-band profiles, the former peak ob-

¹ http://www-utheal.phys.s.u-tokyo.ac.jp/~yamada/soft/XISPileupDoc_20120221/XIS_PileupDoc_20120220.html

Table 1. Log of Suzaku Observation of GRO J1008–57 in the 2012 November Giant Outburst

Date (2012 Nov.)	Obs Time Start/End (UT)	XIS-FI (0.8–10 keV)		HXD-PIN (20–60 keV)		HXD-GSO (60–115 keV)	
		Exp. (ks)	Rate (counts s ⁻¹)	Exp. (ks)	Rate (counts s ⁻¹)	Exp. (ks)	Rate (counts s ⁻¹)
20–22	14:44/05:21	18.09	106.1±0.1	50.38	14.61±0.01	50.38	0.90±0.02

Observation ID = 907006010

**Fig. 2.** Folded pulse profiles by the XIS in 1–10 keV, by HXD-PIN in 10–50 keV, and by HXD-GSO in the 50–70 keV, 70–80 keV, and 80–100 keV bands. The dashed lines divide the pulse cycle into Valley, Rise, Peak, and Fall, referring to the 50–70 keV profile.

tained here is apparently smaller than that in the 2007 outburst.

As illustrated in figure 2, we divided the pulse cycle into four phases, and named them Valley, Rise, Peak, and Fall, according to the profile in the GSO 50–70 keV band. They are used in the phase resolved spectral analysis in section 3.5.

3.3. Cyclotron Resonance Feature in Averaged Spectrum

We examined a pulse-phase-averaged spectrum with the best photon statistics for the previously suggested CRSF signatures. All the spectral fitting attempts hereafter were carried out on Xspec version 12.7.0. The cross normalization factor between the XIS and the HXD was fixed at 1:1.16 according to the latest calibration information². We discard the energy bands of 1.7–1.9 keV around the silicon K edge and 2.1–2.4 keV around the gold M edges in the XIS data, where the calibration uncertainty is relatively larger. We did not use the XIS-BI data either in the

spectral analysis, because it has larger calibration uncertainties than XIS-FI.

Figure 3 (a) shows ratios of the spectra obtained with XIS-FI (0.8–10 keV), HXD-PIN (20–60 keV) and HXD-GSO (60–115 keV) to those of the Crab nebula which has a simple power-law shape with a photon index of ~ 2.1 . Figure 3 (b) shows the count-rate spectra without removing instrument responses. From the Crab ratios, the spectrum is found to be largely approximated by a smooth continuum with cutoffs below ~ 2 keV and above ~ 20 keV. In addition, iron-K emission lines at around 6.5 keV and an edge-like feature at around 70–80 keV are clearly seen. The latter looks like a typical CRSF observed in some XBP spectra, and its energy is close to those of the possible absorption features (~ 88 keV) reported in past outbursts (Shrader et al. 1999; Kühnel et al. 2013).

We fitted the spectrum above 20 keV with typical XBP continuum models; cutoff power-law (CPL, `cutoffpl` in Xspec terminology), FDCO (Fermi-Dirac cutoff power-law; Tanaka 1986), and NPEX (Negative and Positive power laws with EXponential cutoff; Mihara et al. 1998) whose positive power-law index was fixed at 2.0. However, as exemplified in figure 4 (a), none of these models alone were able to fit the data sufficiently, because of the feature at 70–80 keV. We thus applied a cyclotron absorption factor (CYAB; `cyclabs` in Xspec terminology, Mihara et al. 1990, Makishima et al. 1999) to the above continuum models. Since the width W of the CYAB factor cannot be constrained lower than the energy resolution, ~ 5 keV at 80 keV in HXD GSO, we set its lower limit at 2 keV in the model fits. Then, all three continuum models became acceptable within 90% confidence limits, and the improvements of chi-squared (χ^2_ν) for degree of freedom (ν) were estimated with the F-test to be significant above the 99% confidence limit. The case with NPEX * CYAB is shown in figure 4 (b). As listed in table 2, the best-fit CRSF energy, $E_a \sim 75$ –80 keV, slightly depends on the continuum model.

Since the CRSF energy, ~ 80 keV, is rather high, we should examine the possibility that it is in reality the second harmonic. Actually, Vela X-1 has been sometimes reported to show a shallow absorption feature at ~ 25 keV (Makishima et al. 1999), possibly interpreted as the fundamental CRSF, in addition to the more prominent feature at ~ 50 keV which is confirmed in many observations (Mihara et al. 1998; Orlandini et al. 1998; Makishima et al. 1999; Kreykenbohm et al. 1999; Kreykenbohm et al. 2002; Odaka et al. 2013). We hence fitted the Suzaku spectra of GRO J1008–57 by a pair of *harmonic* CYAB factors, with the fundamental resonance energy around ~ 40 keV. Then, as shown in figure 4(c) and given in table 2, the best-fit χ^2_ν slightly decreased to 1.08 from 1.14 of the initial single-CYAB model, yielding $E_1 \sim 37$ keV. However, we consider this harmonic interpretation rather unlikely for the

² <http://www.astro.isas.ac.jp/suzaku/doc/suzakumemo/suzakumemo-2008-06.pdf>

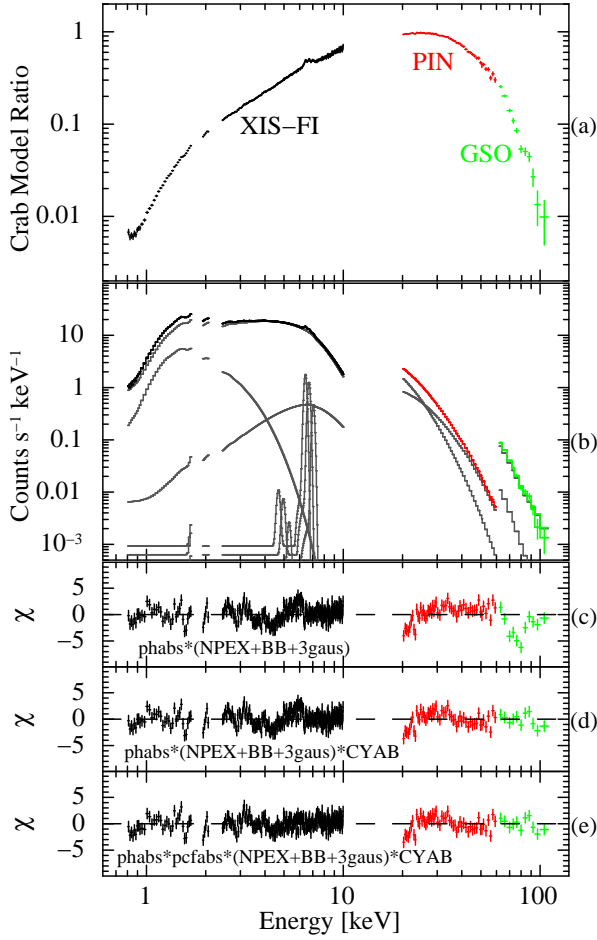


Fig. 3. Pulse-phase-averaged and background-subtracted broadband X-ray spectrum of GRO J1008–57 by Suzaku XIS-FI (0.8–10 keV), HXD-PIN (20–60 keV) and HXD-GSO (60–115 keV). (a) Ratio to the Crab Nebula spectrum. (b) Count-rate spectra and the folded best-fit model of $\text{pcfabs} * \text{phabs} * (\text{NPEX} + \text{BB} + 3\text{gaus}) * \text{CYAB}$. (c) Residuals against $\text{phabs} * (\text{NPEX} + \text{BB} + 3\text{gaus})$ model. (d) Residuals against $\text{phabs} * (\text{NPEX} + \text{BB} + 3\text{gaus}) * \text{CYAB}$ model. (e) Residuals against $\text{pcfabs} * \text{phabs} * (\text{NPEX} + \text{BB} + 3\text{gaus}) * \text{CYAB}$ model.

following reasons. First, such a local feature at ~ 40 keV is not visible in figure 4(b). Second, an F -test indicates that the fit improvement by introducing the second CRSF factor is less significant than 80%. Third, the derived ratio $D_1/D_2 = 0.02$ of GRO J1008–57 is even smaller than that of Vela X-1, $D_1/D_2 = 0.07/0.8 = 0.09$ (Makishima et al. 1999). Finally, the obtained width $W_1 \sim 11$ keV for the lower-energy feature is much wider than those of Vela X-1 ($W_1 \sim 2.2$ keV) and the higher-energy feature of GRO J1008–57 ($W_2 = 2.0$ keV). Therefore, we consider that the deep 75–80 keV feature GRO J1008–57 is the fundamental resonance, although the alternate interpretation, that it is the second harmonic resonance, cannot be completely ruled out.

3.4. Broadband Spectral Model for Averaged Spectrum

Now that the 20–100 keV HXD spectrum was successfully modeled and the CRSF was clearly detected, the next step is to search for broadband emission models that can explain the whole Suzaku spectrum from 0.5 keV to 115 keV. We first

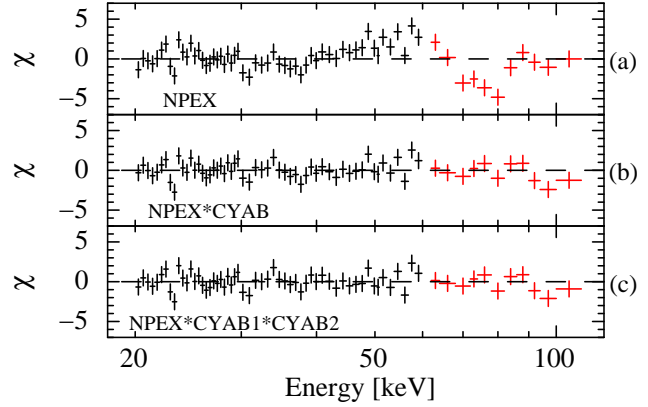


Fig. 4. Data-to-model residuals when the HXD data are fitted with (a) NPEX alone, (b) NPEX * CYAB, and (c) NPEX * CYAB1 * CYAB2 in 20–115 keV band.

tested the CPL, FDCO, and NPEX continuum models as used in the previous section, incorporating a CYAB factor at 75–80 keV and an interstellar absorption (phabs in Xspec terminology) whose hydrogen column density N_H was set free. In any continuum model, however, the fit was far from acceptable, and the data-to-model residuals showed an excess in the soft X-ray band below 3 keV and iron K-lines at around 6.5 keV. This agrees with the results obtained in past outbursts (e.g. Naik et al. 2011; Kühnel et al. 2013).

We then added a blackbody (BB) model to account for the soft X-ray residuals, and three narrow gaussians (gaus) for K_α lines from neutral iron (6.4 keV) and helium-like iron (6.7 keV), as well as K_β line at 7.05 keV. Among the three continuum models, the NPEX-based composite model, expressed by $\text{phabs} * (\text{NPEX} + \text{BB} + 3\text{gaus}) * \text{CYAB}$, fit the data much better than the other two, but it is still unacceptable with $\chi_\nu^2 = 1.80$ for $\nu = 350$ degree of freedom. The residuals, as shown in figure 3 (d), indicate that discrepancy remains at around 4 keV and around 20 keV. To improve the fit, we tried to apply a partially covering absorption model (pcfabs in Xspec terminology). The fit became even better with $\chi_\nu^2 = 1.45$ for $\nu = 348$ as shown in figure 3 (e). However, it is still outside the 90% confidence limit. This may be because the phase-averaged spectrum has complex features that can arise by averaging pulse-phase dependent spectra. Table 3 summarizes all the best-fit model parameters.

3.5. Pulse-Phase Resolved Spectra

As seen in figure 2, the folded pulse profiles from 1 keV to 100 keV are apparently energy dependent. This means that the energy spectrum depends on the pulse phase. We thus extracted four spectra, one from each of the four pulse phases defined in figure 2 from the 50–70 keV GSO pulse profile. Figure 5 shows the obtained four spectra in a form of their ratios to the phase-averaged spectrum. While the spectrum in the Valley phase is softer than the average, that in the Peak phase is harder. No feature are apparent at the iron K-line band around 6–7 keV in these ratio plots. This indicates that the equivalent width of the iron lines does not depend on the pulse phases.

We fitted each phase-resolved spectrum with the model which best described the phase averaged spectrum in section

Table 2. Summary of model fits to Suzaku HXD 20–115 keV spectrum with either CPL, FDCO, or NPEX continuum and zero, one, or two CYABs.

Continuum	CPL			FDCO			NPEX		
	None	1 CYAB	2 CYAB	None	1 CYAB	2 CYAB	None	1 CYAB	2 CYAB
α_1	–0.63	$0.11^{+0.16}_{-0.13}$	$0.49^{+0.64}_{-0.27}$	1.61	$0.69^{+0.67}_{-0.12}$	$0.89^{+0.43}_{-0.35}$	1.25	$0.16^{+0.22}_{-0.22}$	$0.76^{+0.71}_{-0.66}$
E_{cut} (keV)	9.3	$12.6^{+1.2}_{-0.8}$	$16.5^{+3.8}_{-4.2}$	39.0	$0.3^{+28.9}_{-0.3}$	$0.01^{+155}_{-0.01}$	—	—	—
E_{fold}/kT (keV)	—	—	—	10.9	$13.8^{+0.3}_{-0.8}$	$18.3^{+5.3}_{-4.1}$	7.38	$8.15^{+0.671}_{-0.21}$	$7.81^{+0.52}_{-0.18}$
A_1^*	0.03	$0.15^{+0.06}_{-0.04}$	$0.32^{+0.53}_{-0.10}$	3.11	$0.57^{+0.21}_{-0.14}$	$1.25^{+1.93}_{-0.40}$	4.73	$0.24^{+0.20}_{-0.11}$	$1.19^{+2.41}_{-0.98}$
A_2^*	—	—	—	—	—	—	5.2	$2.5^{+0.6}_{-1.2}$	$3.9^{+0.9}_{-1.6}$
D_1	—	$1.44^{+0.20}_{-0.18}$	$0.06^{+0.12}_{-0.03}$	—	$1.50^{+0.21}_{-0.18}$	$0.08^{+0.14}_{-0.04}$	—	$2.96^{+1.06}_{-1.94}$	$0.06^{+0.08}_{-0.03}$
E_{a1} (keV)	—	$79.5^{+2.9}_{-2.2}$	$40.7^{+1.1}_{-1.3}$	—	$80.0^{+2.6}_{-2.0}$	$40.6^{+1.1}_{-1.0}$	—	$74.4^{+2.5}_{-1.3}$	$36.8^{+1.1}_{-0.7}$
W_1 (keV)	—	$13.4^{+6.7}_{-4.9}$	$9.0^{+11.4}_{-9.0}$	—	$14.1^{+4.0}_{-4.0}$	$10.1^{+10.0}_{-8.5}$	—	$2.0^{+6.4}_{-***}$	$11.1^{+7.2}_{-10.2}$
D_2	—	—	$2.01^{+1.13}_{-0.58}$	—	—	$2.08^{+1.16}_{-0.57}$	—	—	$2.63^{+1.0}_{-1.3}$
$E_{a2} = 2E_{a1}$	—	—	81.4	—	—	81.2	—	—	73.6
W_2 (keV)	—	—	$23.7^{+9.5}_{-7.2}$	—	—	$24.2^{+11.2}_{-7.9}$	—	—	$2.0^{+7.7}_{-***}$
χ^2_ν	6.12(64)	1.25(61)	1.24(59)	2.59(63)	1.29(60)	1.02(58)	2.73(63)	1.14(60)	1.08(58)

* Units in photons s^{–1} cm^{–2} keV^{–1} at 1 keV.**Table 3.** Best-fit models for Suzaku 0.8–115 keV broadband spectrum

Component	Parameter	Model Function			
		phabs	phabs	phabs	phabs * pcfabs
		*Cont(CPL) [†]	*Cont(FDCO) [†]	*Cont(NPEX) [†]	*Cont(NPEX) [†]
		*CYAB	*CYAB	*CYAB	*CYAB
phabs	N_{H} (10^{22} cm ^{–2})	1.01	1.07	$0.95^{+0.02}_{-0.01}$	$0.93^{+0.02}_{-0.02}$
bbody	kT_{BB} (keV)	0.36	0.30	$0.41^{+0.01}_{-0.01}$	$0.44^{+0.02}_{-0.02}$
	I_{BB}^* ($\times 10^{-3}$)	5.1	4.8	$6.1^{+0.3}_{-0.3}$	$4.8^{+0.4}_{-0.4}$
gaus1	$E_{\text{Fe K}\alpha}$ (keV)	6.40	6.40	$6.41^{+0.01}_{-0.01}$	$6.42^{+0.01}_{-0.01}$
	$I_{\text{Fe K}\alpha}^*$ ($\times 10^{-3}$)	3.9	4.2	$3.7^{+0.2}_{-0.2}$	$3.0^{+0.3}_{-0.2}$
gaus2	$E_{\text{Fe 6.7}}$ (keV)	6.69	6.69	$6.69^{+0.01}_{-0.01}$	$6.69^{+0.02}_{-0.01}$
	$I_{\text{Fe 6.7}}^*$ ($\times 10^{-3}$)	3.3	3.7	$3.0^{+0.2}_{-0.2}$	$2.3^{+0.2}_{-0.3}$
gaus3	$E_{\text{Fe K}\beta}$ (keV)	7.00	7.01	$7.00^{+0.02}_{-0.02}$	$7.04^{+0.04}_{-0.03}$
	$I_{\text{Fe K}\beta}^*$ ($\times 10^{-4}$)	17.4	21.1	$14.6^{+2.1}_{-2.2}$	$9.5^{+2.2}_{-2.2}$
pcfabs	N_{H} (10^{22} cm ^{–2})	—	—	—	$32.5^{+4.4}_{-4.8}$
	f_{PCF}	—	—	—	$0.18^{+0.02}_{-0.02}$
NPEX	α_1	0.51	0.69	$0.27^{+0.01}_{-0.01}$	$0.38^{+0.03}_{-0.02}$
	E_{cut} (keV)	14.7	0.0	—	—
	kT/E_{fold} (keV)	—	13.8	$8.79^{+0.34}_{-0.23}$	$8.58^{+0.60}_{-0.25}$
	A_1^\dagger ($\times 10^0$)	0.34	0.79	$0.29^{+0.00}_{-0.00}$	$0.39^{+0.02}_{-0.02}$
	A_2^\dagger ($\times 10^{-4}$)	—	—	$1.4^{+0.2}_{-0.2}$	$1.6^{+0.3}_{-0.4}$
CYAB	D	1.55	1.58	$0.88^{+0.39}_{-0.15}$	$0.79^{+1.26}_{-0.14}$
	E_a (keV)	80.2	79.8	$78.1^{+4.1}_{-2.8}$	$78.1^{+7.6}_{-3.6}$
	W (keV)	11.9	6.2	$11.6^{+8.7}_{-6.9}$	$11.8^{+19.7}_{-9.6}$
	χ^2_ν	2.53 (351)	3.91 (350)	1.80 (350)	1.45 (348)
	$L_{0.5-100 \text{ keV}}^\S$	—	—	—	$10.93^{+0.01}_{-0.05}$

* Units in photons s^{–1} cm^{–2}.† Units in photons s^{–1} cm^{–2} keV^{–1} at 1 keV.

‡ Cont(CPL) is a CPL-based composite model including a soft BB and three iron-lines, expressed by CPL + BB + 3gaus.

Cont(FDCO) and Cont(NPEX) represent FDCO-based and NPEX-based composite models, respectively.

§ Units in 10^{37} erg s^{–1}.

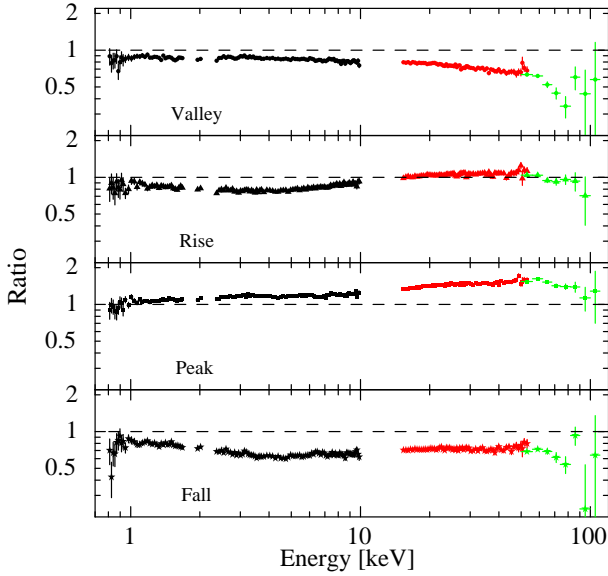


Fig. 5. Pulse-phase resolved spectra for Valley, Rise, Peak, and Fall phases in the form of the ratio to the model that best describes the pulse-phase averaged spectrum.

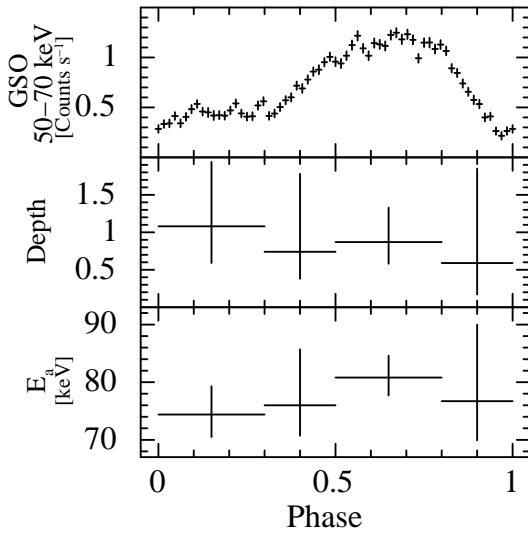


Fig. 6. Pulse-phase dependence of the CRSF depth D and energy E_a . The vertical error bars of D and E_a represent 90% confidence limits of statistical uncertainties.

3.3. Here, we fixed the iron $K\beta$ -line energy at 7.05 keV and the CYAB width at a typical value of 5.0 keV because they were poorly constrained by the data with lower statistics. The fits became acceptable except for the Peak phase. Table 4 summarizes the obtained best-fit parameters in each phase.

Although these model parameters for the continuum are correlated in complex ways, those of the CRSF model are mostly free from them. As shown in figure 6, the derived CRSF parameters show some dependence on the pulse phase, but not more significantly than errors.

Table 5. CRSF measurements in GRO J1008–57.

Outburst	Luminosity* (10^{37} erg s $^{-1}$)	CRSF parameters		
		E_a	W	D
		(keV)		
2012 Nov. [†]	10.93	$76^{+1.9}_{-1.7}$	5 (fix)	$1.08^{+0.25}_{-0.21}$
2007 Dec. [‡]	1.79	86^{+7}_{-5}	8^{+6}_{-4}	2.3 (fix)
1993 Jul. [§]	3.0	88	—	$2.3^{+0.6}_{-0.6}$

* Calculated from the best spectral model in 0.5–100 keV.

† This work, ‡ Kühnel et al. (2013), § Shrader et al. (1999),

4. Discussion

4.1. Possible CRSF Energy Change

We analyzed the broadband X-ray (0.8–115 keV) spectrum of GRO J1008–57 obtained by Suzaku, covering the peak of the giant outburst in 2012 detected by MAXI, and found a significant absorption signature at 75–80 keV (Yamamoto et al. 2013). It can be interpreted as a fundamental CRSF, and reconfirms, with much higher significance, the previous suggestions (Shrader et al. 1999, Kühnel et al. 2013).

Table 5 compares the CRSF parameters and luminosity obtained in this work with those of the previous outbursts, and figure 7 gives its graphical plot. Thus, the CRSF energy might decrease towards higher luminosities, although the presently available information is very limited.

The luminosity dependence of the CRSF energy has been observed in several XBPs. While some of them, 4U 0115+63 (Mihara et al. 1998; Mihara et al. 2004; Nakajima et al. 2006) and V 0332+53 (Tsygankov et al. 2006; Mowlavi et al. 2006; Nakajima et al. 2010), showed negative correlations, others, Her X-1 (Gruber et al. 2001; Staubert et al. 2007) and GX 304–1 (Yamamoto et al. 2011; Klochikov et al. 2012) showed positive. These are explained by variations of the cyclotron-scattering photosphere; it increases by radiation pressure in the super-Eddington luminosity regime (Mihara et al. 1998), while it decreases due to dynamical pressure of the accretion in the sub-Eddington luminosity (Staubert et al. 2007). The luminosity of GRO J1008–57 observed by Suzaku at the peak of the 2012 giant outburst, 1.1×10^{38} erg s $^{-1}$, is close to the Eddington luminosity for the typical neutron-star mass of $1.4M_{\odot}$. Therefore, the possible CRSF energy change suggests such a situation that the accretion mode changed from the sub-Eddington to the super-Eddington regime at that time.

4.2. Magnetic Fields in Binary Pulsars

We now know 18 XBPs in which CRSFs are significantly detected and their parameters are determined well. The CRSF energy of 75–80 keV obtained here from GRO J1008–57 is the highest among them. Therefore, the estimated surface magnetic field, $6.6 \times 10^{12} (1 + z_g)$ G, extends the highest end of their magnetic field distribution. Figure 8 shows the updated distribution of the XBP magnetic field strengths. It is still clustered in a very narrow range of $(1.0 - 6.6) \times 10^{12}$ G, compared to the distribution of a larger number (~ 1000) of single radio pulsars in the ATNF pulsar catalog (Manchester et al. 2005). Although the radio pulsars show considerably broader field distribution, this could be due to the much lower accuracy of their field determinations which assume spin down via mag-

Table 4. Best fit parameters of phase resolved spectra

Component	Parameter	Pulse Phase			
		Valley	Rise	Peak	Fall
phabs	$N_{\text{H1}} (10^{22} \text{ cm}^{-2})$	$1.01^{+0.06}_{-0.06}$	$0.90^{+0.05}_{-0.05}$	$1.01^{+0.04}_{-0.04}$	$0.92^{+0.05}_{-0.05}$
bbody	$kT_{\text{BB}} (\text{keV})$	$0.30^{+0.05}_{-0.03}$	$0.43^{+0.04}_{-0.03}$	$0.36^{+0.04}_{-0.03}$	$0.43^{+0.04}_{-0.03}$
	$I_{\text{BB}} (\times 10^{-3})$	$3.3^{+1.4}_{-1.0}$	$5.5^{+0.7}_{-0.7}$	$4.1^{+0.9}_{-0.8}$	$5.5^{+0.7}_{-0.7}$
gaus ₁	$E_{\text{Fe K}\alpha} (\text{keV})$	$6.40^{+0.04}_{-0.03}$	$6.41^{+0.03}_{-0.03}$	$6.41^{+0.03}_{-0.03}$	$6.43^{+0.02}_{-0.02}$
	$I_{\text{Fe K}\alpha}^* (\times 10^{-3})$	$2.0^{+0.5}_{-0.4}$	$2.6^{+0.6}_{-0.5}$	$2.6^{+0.5}_{-0.5}$	$3.3^{+0.5}_{-0.5}$
gaus ₂	$E_{\text{Fe 6.7}} (\text{keV})$	$6.66^{+0.04}_{-0.03}$	$6.69^{+0.04}_{-0.04}$	$6.68^{+0.04}_{-0.03}$	$6.74^{+0.05}_{-0.05}$
	$I_{\text{Fe 6.7}}^* (\times 10^{-3})$	$1.9^{+0.4}_{-0.5}$	$2.2^{+0.6}_{-0.6}$	$2.0^{+0.5}_{-0.3}$	$1.7^{+0.5}_{-0.5}$
gaus ₃	$I_{\text{Fe K}\beta}^* (\times 10^{-4})$	$6.9^{+3.8}_{-3.9}$	$7.2^{+4.8}_{-4.9}$	$1.3^{+4.5}_{-1.3}$	$6.6^{+4.5}_{-4.5}$
pcfabs	$N_{\text{H2}} (10^{22} \text{ cm}^{-2})$	$48.3^{+6.2}_{-5.9}$	$42.3^{+12.7}_{-14.7}$	$53.8^{+7.0}_{-6.2}$	$41.6^{+8.4}_{-10.3}$
	f_{PCF}	$0.23^{+0.04}_{-0.05}$	$0.18^{+0.06}_{-0.07}$	$0.22^{+0.04}_{-0.04}$	$0.28^{+0.06}_{-0.06}$
NPEX	α_1	$0.48^{+0.04}_{-0.04}$	$0.24^{+0.05}_{-0.05}$	$0.41^{+0.03}_{-0.03}$	$0.40^{+0.06}_{-0.06}$
	$kT (\text{keV})$	$7.78^{+0.15}_{-0.13}$	$8.08^{+0.15}_{-0.13}$	$8.11^{+0.07}_{-0.07}$	$8.03^{+0.17}_{-0.14}$
	$A_1^\dagger (\times 10^0)$	$0.46^{+0.05}_{-0.05}$	$0.26^{+0.04}_{-0.04}$	$0.54^{+0.05}_{-0.05}$	$0.30^{+0.06}_{-0.05}$
	$A_2^\dagger (\times 10^{-4})$	$2.0^{+0.2}_{-0.2}$	$2.5^{+0.3}_{-0.3}$	$3.8^{+0.2}_{-0.2}$	$1.8^{+0.2}_{-0.2}$
CYAB	D	$1.08^{+0.86}_{-0.49}$	$0.74^{+1.04}_{-0.36}$	$0.87^{+0.46}_{-0.29}$	$0.59^{+1.26}_{-0.42}$
	$E_a (\text{keV})$	$74.4^{+4.9}_{-3.9}$	$76.0^{+9.7}_{-5.3}$	$80.8^{+3.8}_{-3.1}$	$76.7^{+13.3}_{-6.8}$
	$\chi^2_\nu (\nu)$	1.13 (171)	0.99 (171)	1.49 (171)	1.07 (171)
	$L_{0.5-100 \text{ keV}}^\ddagger$	$8.86^{+0.04}_{-0.09}$	$11.10^{+0.04}_{-0.13}$	$15.66^{+0.05}_{-0.09}$	$8.00^{+0.04}_{-0.16}$

Spectral model function: phabs * pcfabs * (NPEX + BB + 3gaus) * CYAB

Energy of iron $\text{K}\beta$ is fixed to 7.05 keV. Width of CYAB is fixed to 5.0 keV.

* Units in photons $\text{s}^{-1} \text{cm}^{-2}$.

† Units in photons $\text{s}^{-1} \text{cm}^{-2} \text{keV}^{-1}$ at 1 keV.

‡ Units in $10^{37} \text{erg s}^{-1}$.

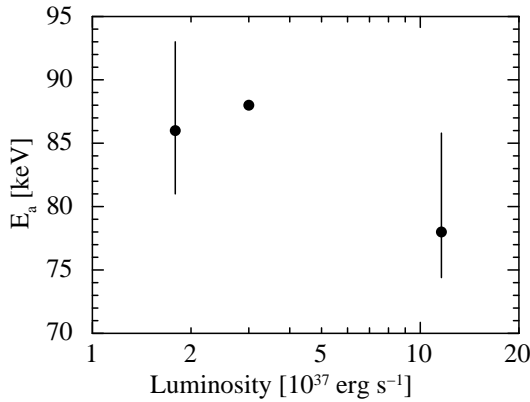


Fig. 7. Luminosity (0.5–100 keV) dependence of the CRSF energy from table 5.

netic dipole radiation. In any case, the plots favor the scenario that the surface magnetic fields of neither XBP nor radio pulsars would decay significantly within their lifetime of $\sim 10^8$ yr (Itoh et al. 1995; Makishima et al. 1999).

GRO J1008–57 is known to have a large orbital eccentricity of $e = 0.68(2)$ (Coe et al. 2007). In figure 9, we plot a relation between the surface magnetic fields and orbital eccentricities of 15 XBPs whose CRSFs and binary orbital parameters are well determined. On this plot, GRO J1008–57 locates at the upper right corner. Thus, the surface magnetic field and the orbital eccentricity of high mass X-ray binaries, including BeXBs, appear to have a positive correlation. This may suggest the evolutionary relation between these parameters. Since the surface magnetic fields would not change as discussed above and the

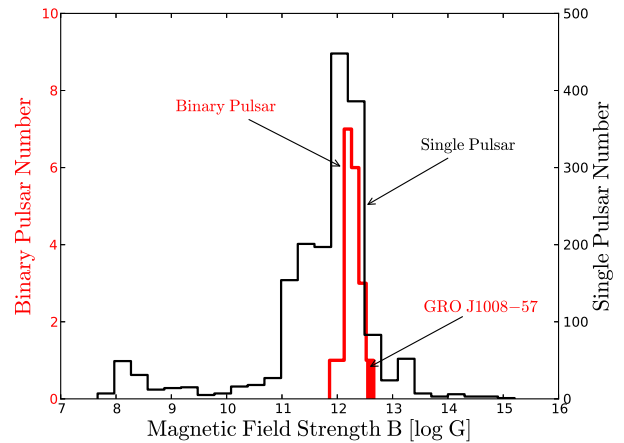


Fig. 8. Distribution of magnetic field strengths on neutron stars in binary pulsars estimated from the CRSFs (red ordinate to the left) and in single pulsars from the period and the period derivative from ATNF pulsar catalog (Manchester et al. 2005) (black, to the right). It is updated from those in Mihara et al. (1998) and Makishima et al. (1999).

orbital eccentricity would not change significantly within their lifetime, the correlation is considered to be formed when the XBPs are born. Further observational as well as theoretical studies are necessary.

We thank the Suzaku operation team for arranging and carrying out the TOO observations. We are also grateful to all members of the MAXI and the ISS-operation teams. This research was partially supported by the Ministry of Education,

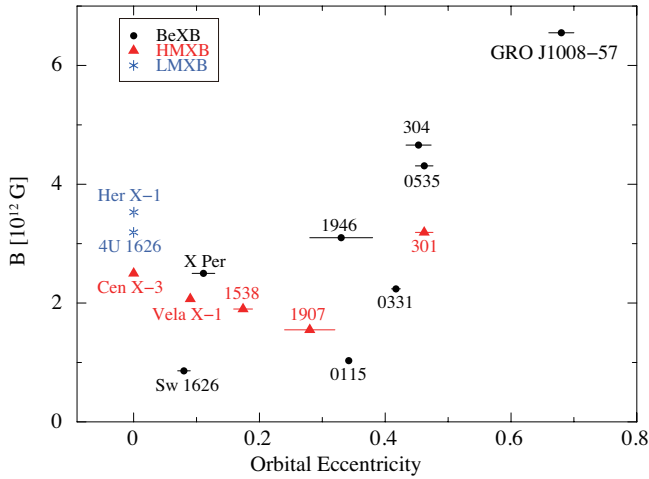


Fig. 9. The magnetic field strengths of XBP's measured with the CRSF technique, plotted against their orbital eccentricities. Meanings and references of labels to the data points are as follows : GRO J1008–57 (This work; Coe et al. 2007), 304 (GX 304–1; Yamamoto et al. 2011; Yamamoto 2013; Yamamoto et al. in prep.), 0535 (A 0535+26; Caballero et al. 2013; Finger et al. 1994), Her X–1 (Vasco et al. 2011; Staubert et al. 2009), 4U 1626 (4U 1626–67; Iwakiri et al. 2012; Chakrabarty et al. 1997), 301 (GX 301–2; Suchy et al. 2012; Koh et al. 1997), 1946 (XTE J1946+274 ; Maitra & Paul 2013; Wilson et al. 2003), X Per (Coburn et al. 2001; Delgado-Martí et al. 2001), Cen X–3 (Suchy et al. 2008; Raichur & Paul 2010), 0331 (X0331+53; Nakajima et al. 2010; Raichur & Paul 2010), Vela X–1 (Odaka et al. 2013; Bildsten et al. 1997), 1538 (4U 1538–52; Rodas-Roca et al. 2009; Clark 2000), 1907 (4U 1907+09; Rivers et al. 2010; Baykal et al. 2006), 0115 (4U 0115+63; Nakajima et al. 2006; Raichur & Paul 2010), Sw 1626 (Swift J1626.6–5156; DeCesar et al. 2013).

Culture, Sports, Science and Technology (MEXT), Grant-in-Aid No. 24340041 and 23244024.

References

- Baykal, A., İnam, S. Ç., & Beklen, E. 2006, *MNRAS*, 369, 1760
- Bildsten, L., et al. 1997, *ApJS*, 113, 367
- Caballero, I., et al. 2013, *ApJL*, 764, L23
- Chakrabarty, D., et al. 1997, *ApJ*, 474, 414
- Clark, G. W. 2000, *ApJL*, 542, L131
- Coburn, W., Heindl, W. A., Gruber, D. E., Rothschild, R. E., Staubert, R., Wilms, J., Kreykenbohm, I., 2001, *ApJ*, 552, 738
- Coburn, W., Heindl, W. A., Rothschild, R. E., Gruber, D. E., Kreykenbohm, I., Wilms, J., Kretschmar, P., & Staubert, R., 2002, *ApJ*, 580, 394
- Coe, M. J., et al. 1994, *MNRAS*, 270, L57
- Coe, M. J., et al. 2007, *MNRAS*, 378, 1427
- DeCesar, M. E., Boyd, P. T., Pottschmidt, K., Wilms, J., Suchy, S., Miller, M. C., 2013, *ApJ*, 762, 61
- Delgado-Martí, H., Levine, A. M., Pfahl, E., & Rappaport, S. A. 2001, *ApJ*, 546, 455
- Doroshenko, V., Suchy, S., Santangelo, A., Staubert, R., Kreykenbohm, I., Rothschild, R. E., Pottschmidt, K., Wilms, J., 2010, *A&A*, 515, L1
- Filippova, E. V., Tsygankov, S. S., Lutovinov, A. A., & Sunyaev, A. A. 2007, *ESA Special Publication*, 622, 449
- Finger, M. H., Wilson, R. B., & Hagedorn, K. S. 1994, *IAU Circ.*, 5931, 1
- Fukazawa, Y., et al. 2009, *PASJ*, 61, 17
- Gruber, D. E., Heindl, W. A., Rothschild, R. E., Coburn, W., Staubert, R., Kreykenbohm, I., & Wilms, J. 2001, *ApJ*, 562, 499
- Itoh, N., Kotouda, T., & Hiraki, K. 1995, *ApJ*, 455, 244
- Iwakiri, W. B., et al. 2012, *ApJ*, 751, 35
- Klochkov, D., et al. 2012, *A&A*, 542, L28
- Koh, D. T., et al. 1997, *ApJ*, 479, 933
- Kokubun, M., et al. 2007, *PASJ*, 59, 53
- Koyama, K., et al. 2007, *PASJ*, 59, 23
- Kreykenbohm, I., Kretschmar, P., Wilms, J., Staubert, R., Kendziorra, E., Gruber, D. E., Heindl, W. A., Rothschild, R. E., 1999, *A&A*, 341, 141
- Kreykenbohm, I., Coburn, W., Wilms, J., Kretschmar, P., Staubert, R., Heindl, W. A., Rothschild, R. E., 2002, *A&A*, 395, 129
- Kuehnel, M., et al. 2012, *The Astronomer's Telegram*, 4577, 1
- Kühnel, M., et al. 2013, *A&A*, 555, A95
- Maitra, C., & Paul, B. 2013, *ApJ*, 771, 96
- Makishima, K., Mihara, T., Nagase, F. & Tanaka, Y., 1999, *ApJ*, 525, 978
- Manchester, R. N., Hobbs, G. B., Teoh, A., & Hobbs, M. 2005, *AJ*, 129, 1993
- Matsuoka, M., et al. 2009, *PASJ*, 61, 999
- Mihara, T., Ph.D. thesis in University of Tokyo 1995
- Mihara, T., et al. 2011, *PASJ*, 63, 623
- Mihara, T., Makishima, K., & Nagase, F., 1998, *Advances in Space Research*, 22, 987
- Mihara, T., Makishima, K., & Nagase, F., 2004, *ApJ*, 610, 390
- Mihara, T., Makishima, K., Ohashi, T., Sakao, T., & Tashiro, M. 1990, *Nature*, 346, 250
- Mowlavi, N., et al. 2006, *A&A*, 451, 187
- Nakajima, M., et al. 2012, *The Astronomer's Telegram*, 4561, 1
- Nakajima, M., Mihara, T., & Makishima, K. 2010, *ApJ*, 710, 1755
- Nakajima, M., Mihara, T., Makishima, K., & Niko, H. 2006, *ApJ*, 646, 1125
- Naik, S., Paul, B., Kachhara, C., Vadawale, S., V. 2011, *MNRAS*, 413, 241
- Odaka, H., Khargulyan, D., Tanaka, Y. T., et al. 2013, *ApJ*, 767, 70
- Orlandini, M., et al. 1998, *A&A*, 332, 121
- Raichur, H., & Paul, B. 2010, *MNRAS*, 401, 1532
- Raichur, H., & Paul, B. 2010, *MNRAS*, 406, 2663
- Reig, P. 2011, *Ap&SS*, 332, 1
- Riquelme, M. S., Torrejón, J. M., & Negueruela, I. 2012, *A&A*, 539, A114
- Rivers, E., et al. 2010, *ApJ*, 709, 179
- Rodas-Roca, J. J., Torrejón, J. M., Kreykenbohm, I., Martinez, N. S., Camero-Arranz, A., Bernabeu, G., 2009, *A&A*, 508, 395
- Shrader, C. R., Sutaria, F. K., Singh, K. P., & Macomb, D. J. 1999, *ApJ*, 512, 920
- Staubert, R., Klochkov, D., & Wilms, J. 2009, *A&A*, 500, 883
- Staubert, R., Shakura, N. I., Postnov, K., Wilms, J., Rothschild, R. E., Coburn, W., Rodina, L., & Klochkov, D. 2007, *A&A*, 465, L25
- Stollberg, M. T., Finger, M. H., Wilson, R. B., et al. 1993, *IAU Circ.*, 5836, 1
- Suchy, S., et al. 2008, *ApJ*, 675, 1487
- Suchy, S., Fürst, F., Pottschmidt, K., Caballero, I., Kreykenbohm, I., Wilms, J., Markowitz, A., Rothschild, R. E., 2012, *ApJ*, 745, 124
- Sugizaki, M., et al. 2011, *PASJ*, 63, 635
- Takahashi, T., et al. 2007, *PASJ*, 59, 35
- Tanaka, Y. 1986, *IAU Colloq. 89: Radiation Hydrodynamics in Stars and Compact Objects*, 255, 198
- Truemper, J., Pietsch, W., Reppin, C., Voges, W., Staubert, R., Kendziorra, E., 1978, *ApJL*, 219, L105
- Tsygankov, S. S., Lutovinov, A. A., Churazov, E. M., & Sunyaev, R. A. 2006, *MNRAS*, 371, 19

- Tsygankov, S. S., Krivonos, R. A., & Lutovinov, A. A. 2012, *MNRAS*, 421, 2407
- Vasco, D., Klochkov, D., & Staubert, R. 2011, *A&A*, 532, A99
- Verbunt, F. 1993, *ARA&A*, 31, 93
- White, N., Swank, J., & Holt, S. S., 1983, *ApJ*, 270, 711
- Wilson, C. A., Finger, M. H., Coe, M. J., & Negueruela, I. 2003, *ApJ*, 584, 996
- Yamada, S., Uchiyama, H., Dotani, T., et al. 2012, *PASJ*, 64, 53
- Yamamoto, T., Ph.D. thesis in Nihon University 2013
- Yamamoto, T., et al. 2011, *PASJ*, 63, 751
- Yamamoto, T., et al. 2013, *The Astron. Telegram*, 4759, 1